Supplementary Material of a **Research Article** published in SEISMICA

# Forecasting 3D Rupture Dynamics of the Alto Tiberina Low-Angle Normal Fault, Italy

**Mathilde Marchandon** * [1], **Alice-Agnes Gabriel** [2], **Lauro Chiaraluce** [3], **Elisa Tinti** [4,3], **Emanuele Casarotti** [3], **James Biemiller** [5]

[1]Ludwig-Maximilians-Universität München, Munich, Germany, [2]Scripps Institution of Oceanography, UC San Diego, La Jolla, USA, [4]Sapienza University of Rome, Rome, Italy, [3]Istituto Nazionale di Geofisica e Vulcanologia, Roma, Italy, [5]USGS, Portland, Oregon, USA

Author contributions: *Conceptualization*: MM,AG,LC,ET,EC. *Methodology*: MM,AG,LC,ET,EC,JB. *Software*: MM,AG. *Validation*: MM,AG,LC,ET,EC,JB. *Formal Analysis*: MM. *Investigation*: MM. *Resources*: AG,LC. *Writing - Original draft*: MM. *Writing - Review & Editing*: MM,AG,JB,ET,EC,LC. *Visualization*: MM. *Supervision*: AG. *Project administration*: AG. *Funding acquisition*: AG,LC,EC.

## Contents of this file



## Text S1: 3D geometry estimation of the secondary faults

We used the seismicity catalog of Valoroso et al. (2017) to build the non-planar geometry of the secondary faults. We proceeded as follows: (i) for each secondary fault, we first measured regularly spaced cross-sections (Figure S1). The cross-sections are 1 km-spaced and all earthquakes located within $\pm$ 500 m of the cross sections are plotted. (ii) On each cross section, we manually picked two points that materialize the fault plane (black line on the cross-sections, Figure S1). We extrapolated the black line to a given upper depth (red points on the cross sections, the upper depth corresponds to the average upper depth of the black lines). Plotted on the map, the alignment of the red points gives the strike of the fault (red points on the map, Figure S1). (iii) After making sure the cross-sections are perpendicular to the estimated segment strike, we measured the dip angle of the alignment on each cross section (black line, Figure S1). (iv) Using the estimated average upper and lower depths and the dip angle values measured along strike, we defined several along-dip contour lines that we used to build the segment non-planar surface. We use this method to estimate the 3D geometry of the Pietralunga segment, as well as the antithetic and synthetic Gubbio segments. The 3D geometry of the Alto Tiberina fault system is shown in Figure 2 of the main paper.

## Text S2: Dynamic relaxation step and data-constrained initial stress

We compute the static stress change rate tensor $SCr_{ij}$ with $i$ and $j = x, y, z$ associated with the slip deficit map using a dynamic relaxation approach. The dynamic relaxation approach consists in imposing the slip-rate of a kinematic model as a boundary condition on a fault plane to obtain the shear-stress history on the fault (e.g. Tinti et al., 2005; Causse et al., 2014). Here, we are interested in the static stress change rate associated with the slip deficit map. We therefore use an arbitrary slip-rate function (a regularized Yoffe function of 1s) in the dynamic relaxation step. The advantage of using the dynamic relaxation approach of SeisSol instead of computing directly the static stress change is that it ensures using the same computational mesh, fault geometries, and material parameters as in the dynamic rupture simulation, avoiding any artifacts or inconsistencies that could arise from using two different software to obtain the static stress rate.

*Corresponding author: M.Marchandon@lmu.de

We multiply the six components of the stress change rate tensor $SCr_{ij}$ by the parameter $T$ (see section 3.3.2 in the main text) to obtain the shear stress change tensor $SC_{ij}$.

$$SC_{ij} = T * SCr_{ij} \tag{1}$$

We then add the six components of the static stress change tensor $SC_{ij}$ to the background Andersonian stress tensor $A_{ij}$ computed with R=0 (meaning that the pre-stress level on the fault is only due to the static stress change) to obtain the data-constrained initial stress tensor $S_{ij}$:

$$S_{xx} = A_{xx} + SC_{xx} \tag{2}$$
$$S_{yy} = A_{yy} + SC_{yy} \tag{3}$$
$$S_{zz} = A_{zz} + SC_{zz} \tag{4}$$
$$S_{xy} = A_{xy} + SC_{xy} \tag{5}$$
$$S_{yz} = A_{yz} + SC_{yz} \tag{6}$$
$$S_{xz} = A_{xz} + SC_{xz} \tag{7}$$
$$\tag{8}$$

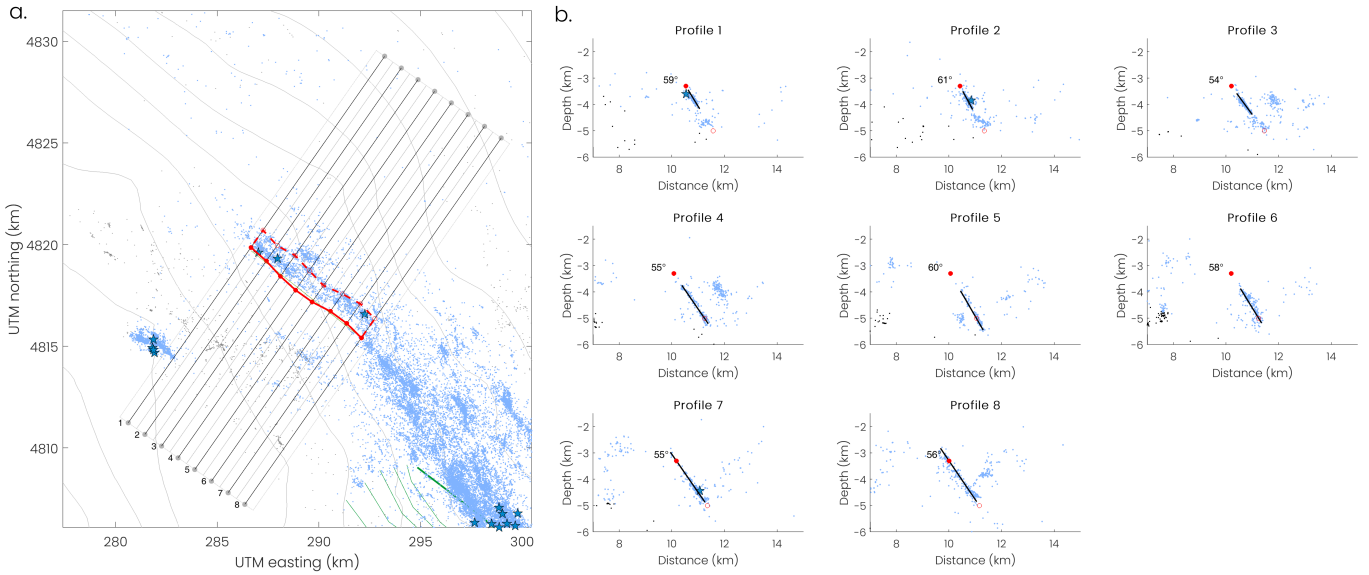


**Figure S1** Estimation of the 3D geometry of the Pietralunga fault from the seismicity catalog of Valoroso et al. (2017). The same method is used for the other secondary faults. (a) Blue and black points show the seismic events within the hanging wall of the Alto Tiberina fault and on the Alto Tiberina fault, respectively (Valoroso et al., 2017). Blue stars denotes the Mw>3.2 events. Gray and green non-linear lines in the background are the depth-contours of the Alto Tiberina and Gubbio faults, respectively (Mirabella et al., 2004, 2011). Black lines show the location of the 8 1 km-spaced cross-sections used to estimate the Pietralunga fault geometry. For each cross-section, all events located within the area delineated by the dotted gray lines are used. The filled and open red circles locate the average upper and lower depth of the seismic alignment estimated from the cross-sections shown in b (see text S1 for details). The red line shows the contour of the estimated geometry with the bold line denoting the upper bound. (b) Cross-sections showing the seismicity alignments used to estimate the geometry of the Pietralunga fault. On each cross-section, the black line highlights the seismicity alignment. The upper and lower depths of the black lines are used to calculate the average upper and lower depths of the Pietralunga fault (filled and open red circles). The non-planar geometry is estimated from the variable dip angles estimated from the black line on each cross-section (the dip angle value is indicated on the cross-sections).

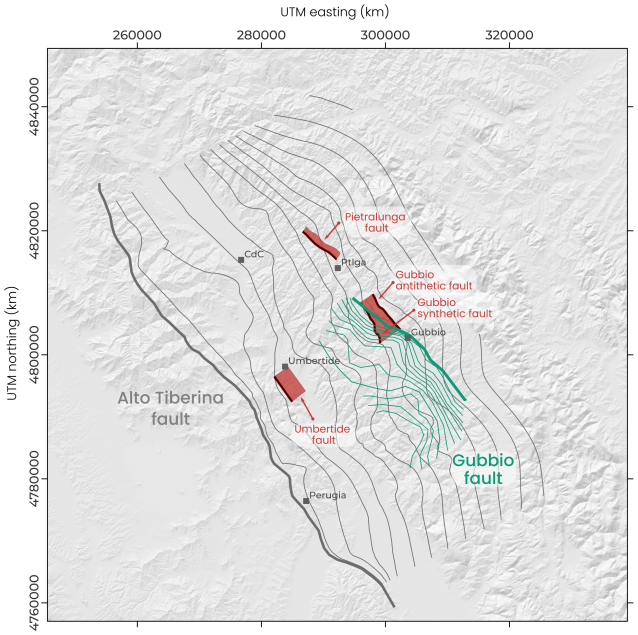


**Figure S2** Map view of the seismically constrained secondary faults included in the modeling. Topographic data are from NASA Shuttle Radar Topography Mission (SRTM) (2013).

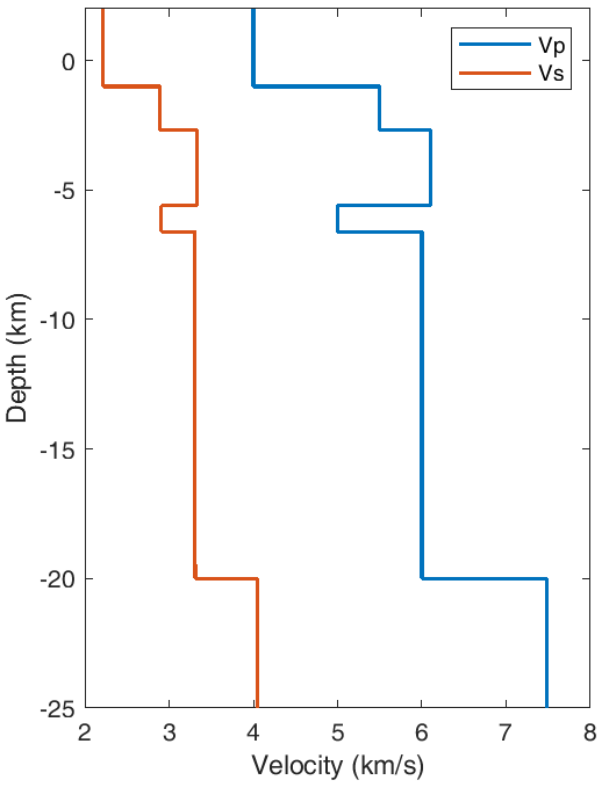


**Figure S3** 1D velocity model from Latorre et al. (2016) adopted in this study.

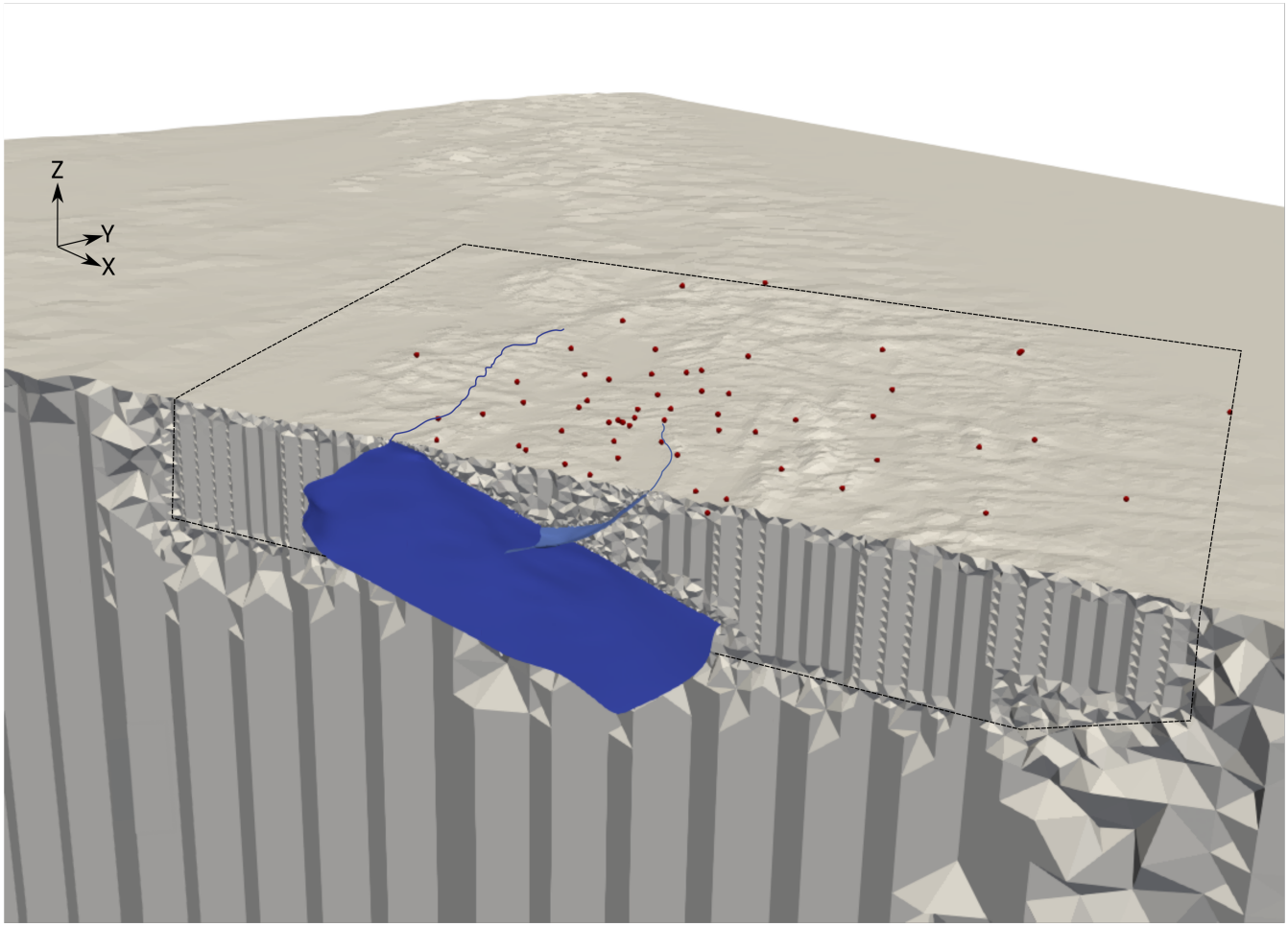


**Figure S4** Cut-out view of the computational mesh that includes the topography from the Shuttle Radar Topography mission (SRTM) Digital Elevation Model (Farr et al., 2007), the Alto Tiberina and Gubbio faults (blue surfaces and lines), as well as four other secondary faults (not visible in this figure, see main text and Figure S1). The black lines outline the $110 \times 110 \times 17$ km$^3$ high-resolution area within which frequencies of at least 1 Hz are resolved, acknowledging the 1D velocity model (Figure S3). Frequencies of at least 0.25 Hz are resolved outside this area. Red dots locate the TABOO-NFO seismic stations.

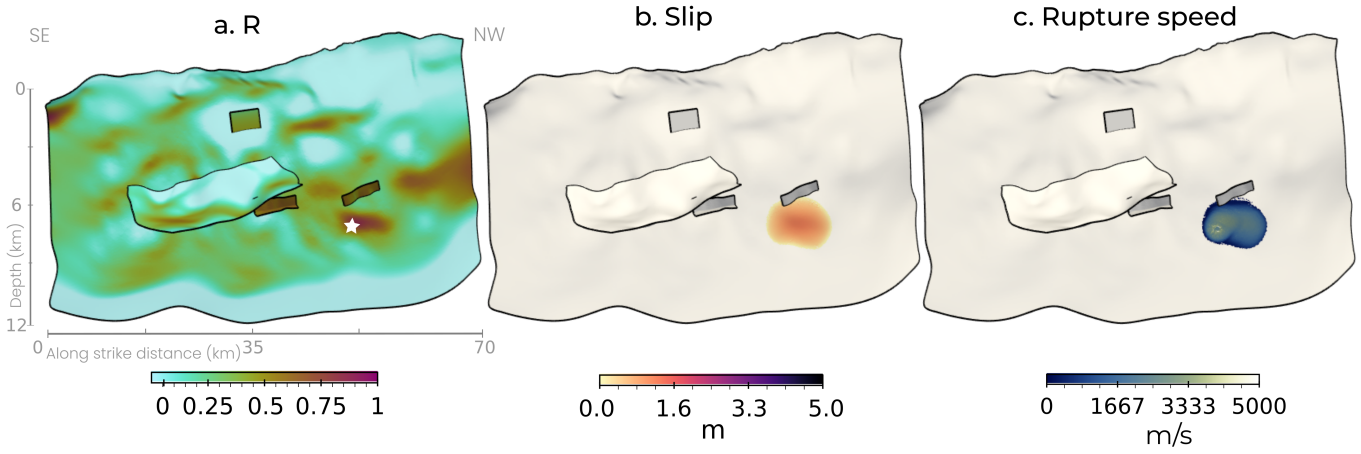


**Figure S5** (a) Pre-stress level, (b) final slip and (c) rupture speed for an homogeneous scenario with pre-stress level $R_0$=0.60. Other parameters are identical to the reference model (Table 1 in the main paper). The white star on panel (a) locates the nucleation location.

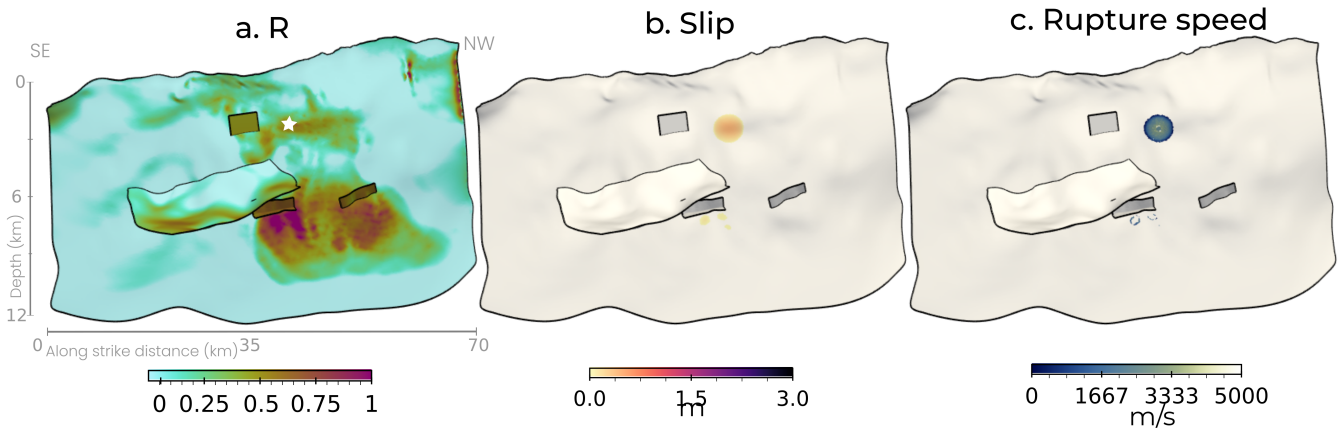


**Figure S6** (a) Pre-stress level $R$, (b) final slip and (c) rupture speed for the heterogeneous scenario when the nucleation is located in the second main stressed patch. Other parameters are identical to the heterogeneous model shown in the main paper. The white star on panel (a) locates the nucleation location.

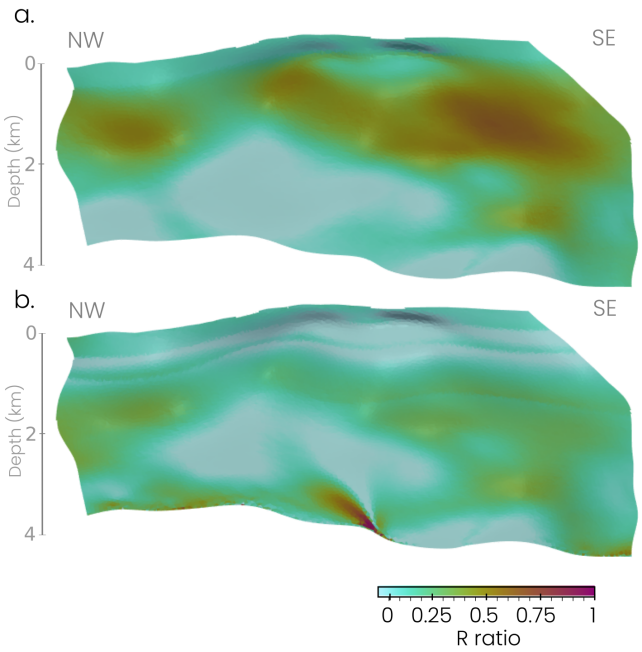


**Figure S7** $R$ ratio distribution on the Gubbio fault for the homogeneous reference scenario at (a) the first time step t=0 and (b) at the end of the simulation.

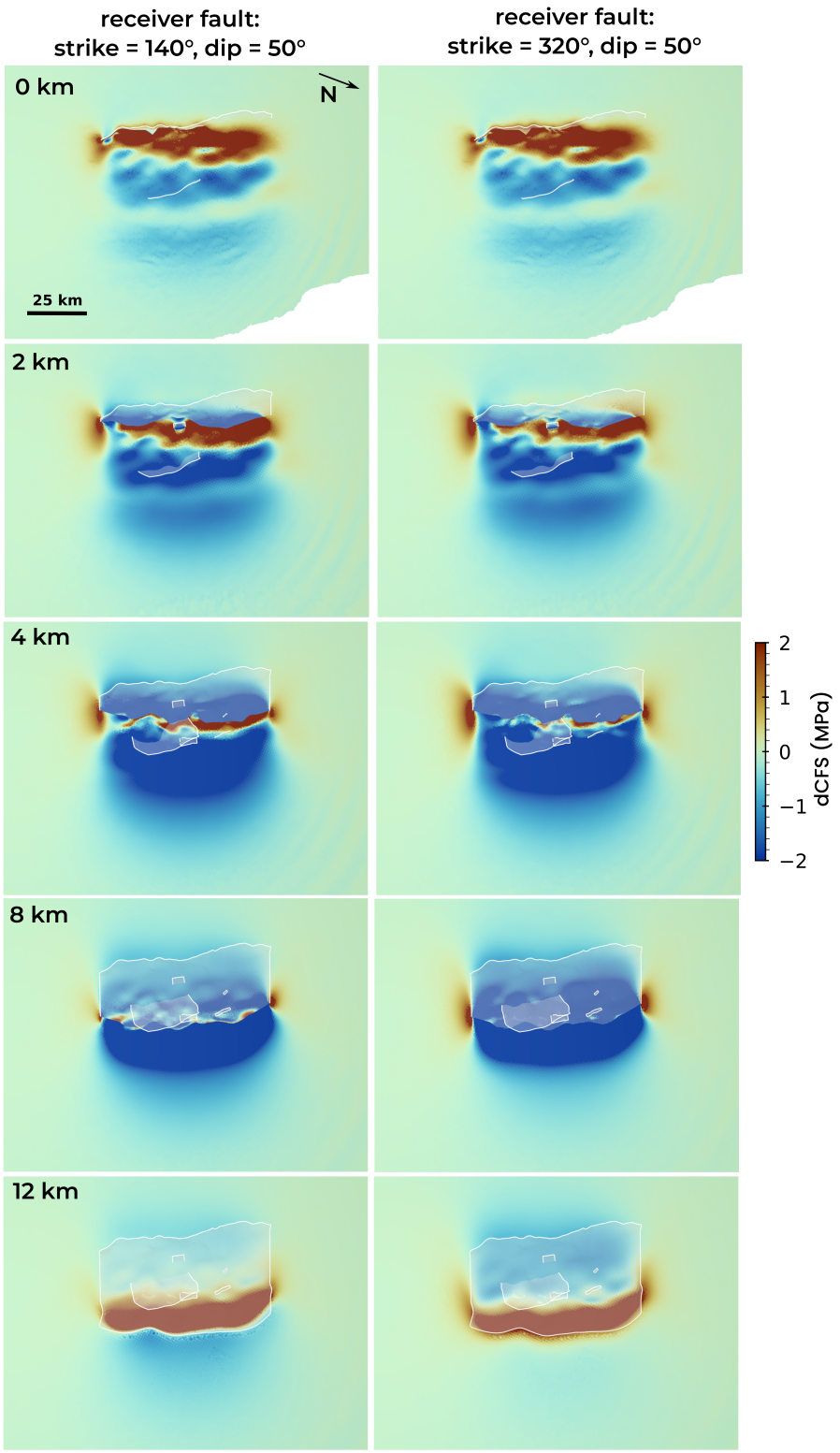


**Figure S8** Static Coulomb stress changes (dCFS) maps at various depths induced by the reference homogeneous scenario (Figure 4b and Table 1) and assuming as receivers 50°-dipping antithetic (left panels) and synthetic (right panels) faults to the ATF.

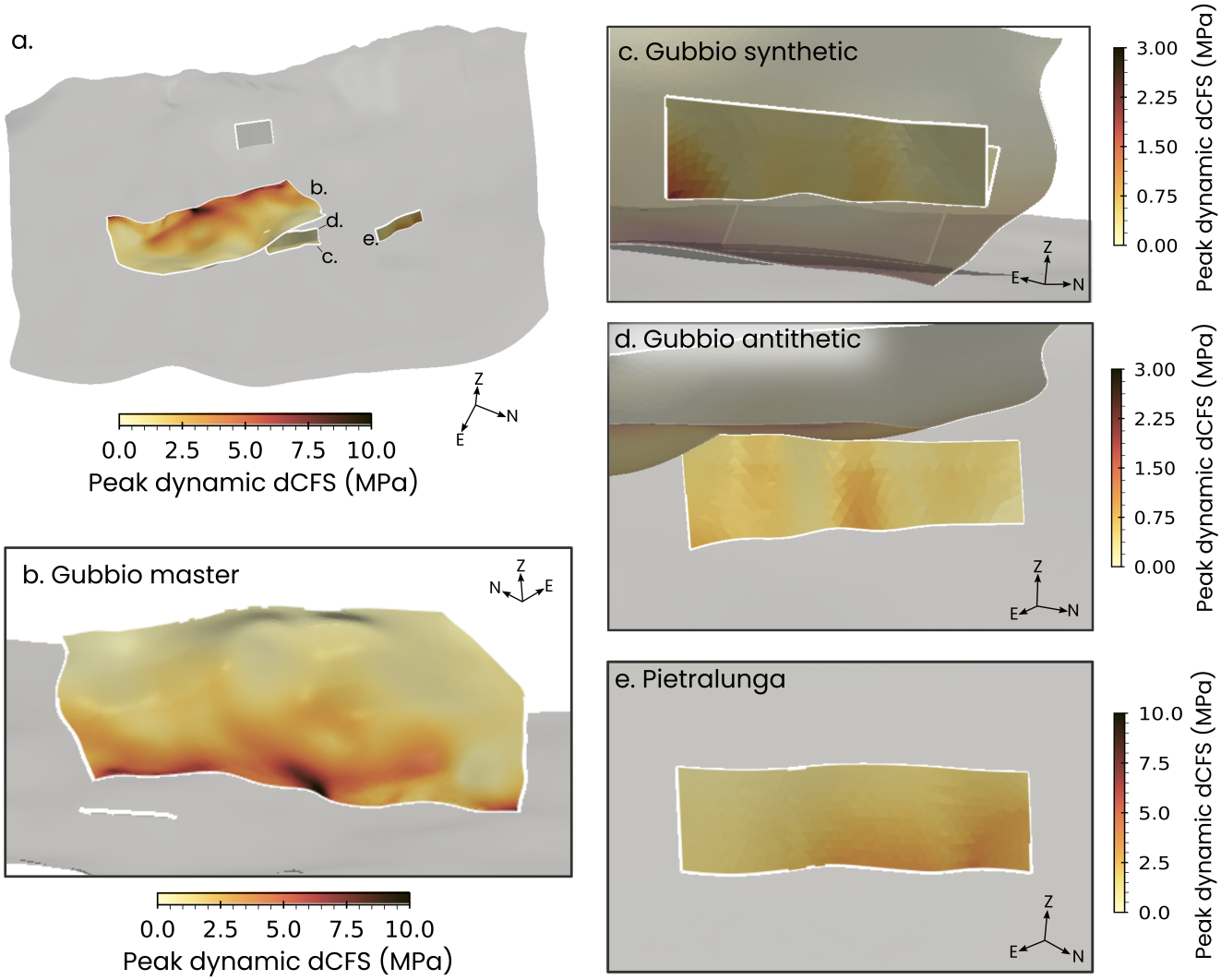


**Figure S9** (a) Peak dynamic Coulomb stress changes induced by the homogeneous reference scenario (Figure 4b and Table 1) on the Alto Tiberina fault system. The Alto Tiberina fault and the Umbertide fault, that both break during the reference scenario, are plotted in gray with a lower opacity level to highlight the other faults. (b-e) Close-up views on the other faults. On panel d, the Gubbio synthetic segment is not plotted for visibility.

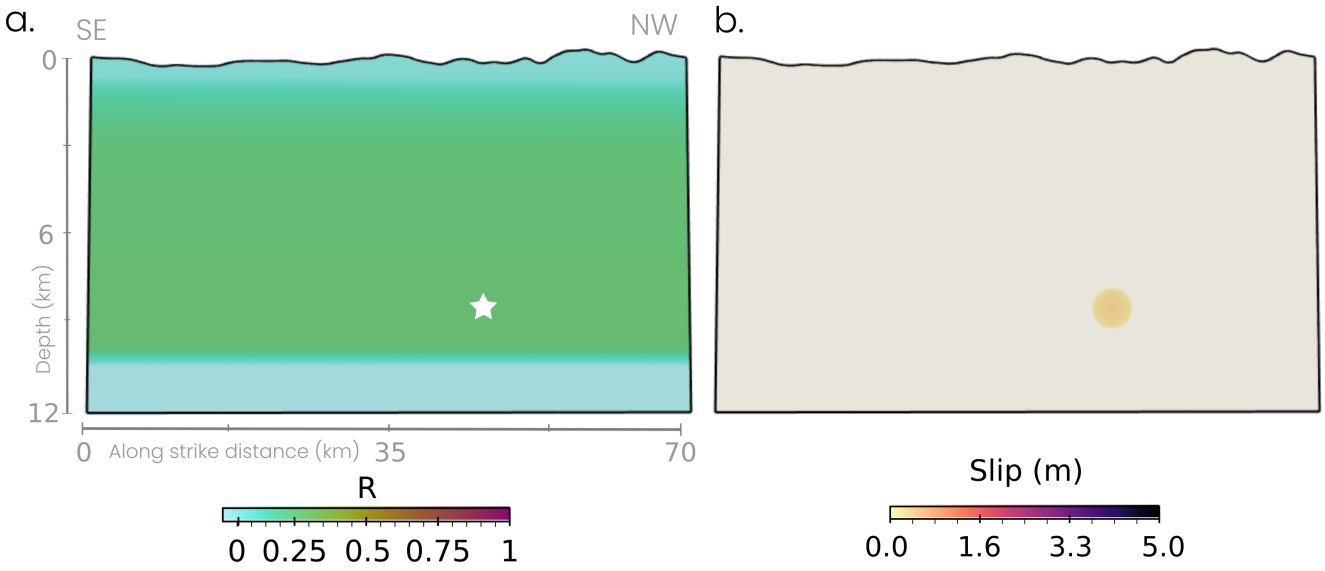


**Figure S10** Dynamic rupture scenario in which the Alto Tiberina fault is modeled as a 17° dipping planar fault. The initial conditions are the same as for the homogeneous reference scenario ($R_0$=0.70, $\mu_s$=0.37, $D_c$=0.4, Table 1 and Figure 4 in the main paper). (a) Pre-stress level distribution $R$. The white star locates the nucleation location. (b) Final slip amplitude.

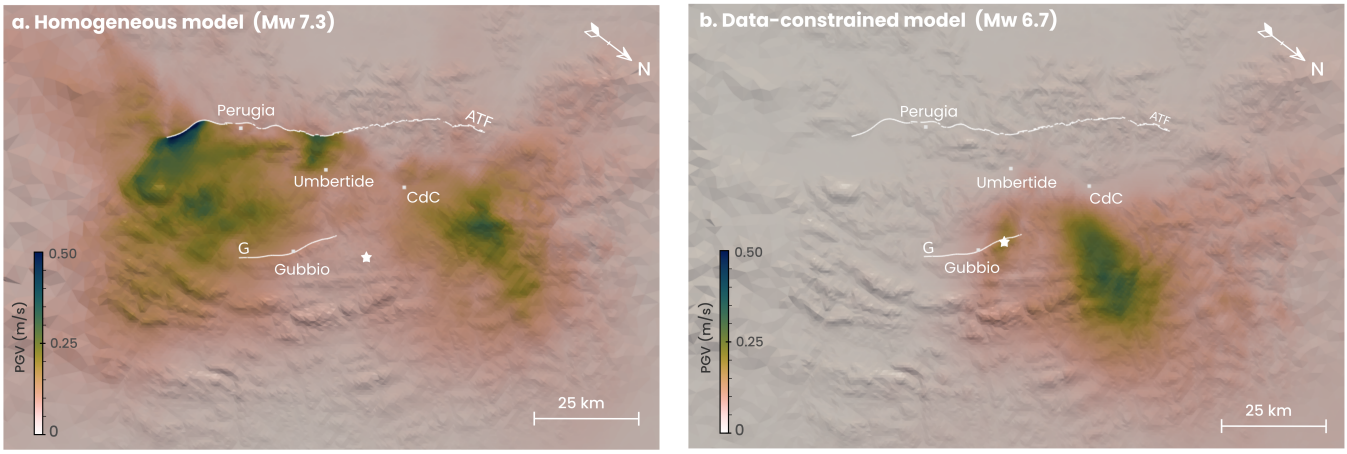


**Figure S11** Map of the synthetic Peak Ground Velocities (PGVs) for (a) the homogeneous reference model ($R_0$=0.70, $\mu_s$=0.37) and (b) the data-constrained model. The squares locate the Perugia, Umbertide, Gubbio and Città di Castillo (CdC) towns. The white lines show the surface traces of the Alto Tiberina (ATF) and Gubbio master (G) faults. The white star locates the epicenter. For the reference homogeneous scenario (Mw 7.3), the bilateral rupture leads to two main areas of high PGV (>0.25m/s, panel a), located north-east and south of the epicenter, respectively. The maximum PGV of ∼1.5 m/s is found at the fault trace on the SE part of the fault where the surface rupturing associated with a local steepening of the fault dip angle amplify locally the ground motions. For this scenario, the cities of Perugia, Umbertide, Gubbio and Città di Castello undergo moderate PGVs of 0.09 m/s, 0.15 m/s, 0.1 m/s, and 0.1 m/s, respectively. The unilateral rupture of the data-constrained scenario (Mw 6.7) leads to one main lobe of high PGV values (>0.17 m/s) located NNE of the epicenter (panel b) with a maximum PGV of ∼0.3 m/s. For this scenario, the Perugia, Umbertide, Gubbio, and Città di Castello towns undergo PGV lower than 0.06 m/s. Topographic data are from NASA Shuttle Radar Topography Mission (SRTM) (2013).

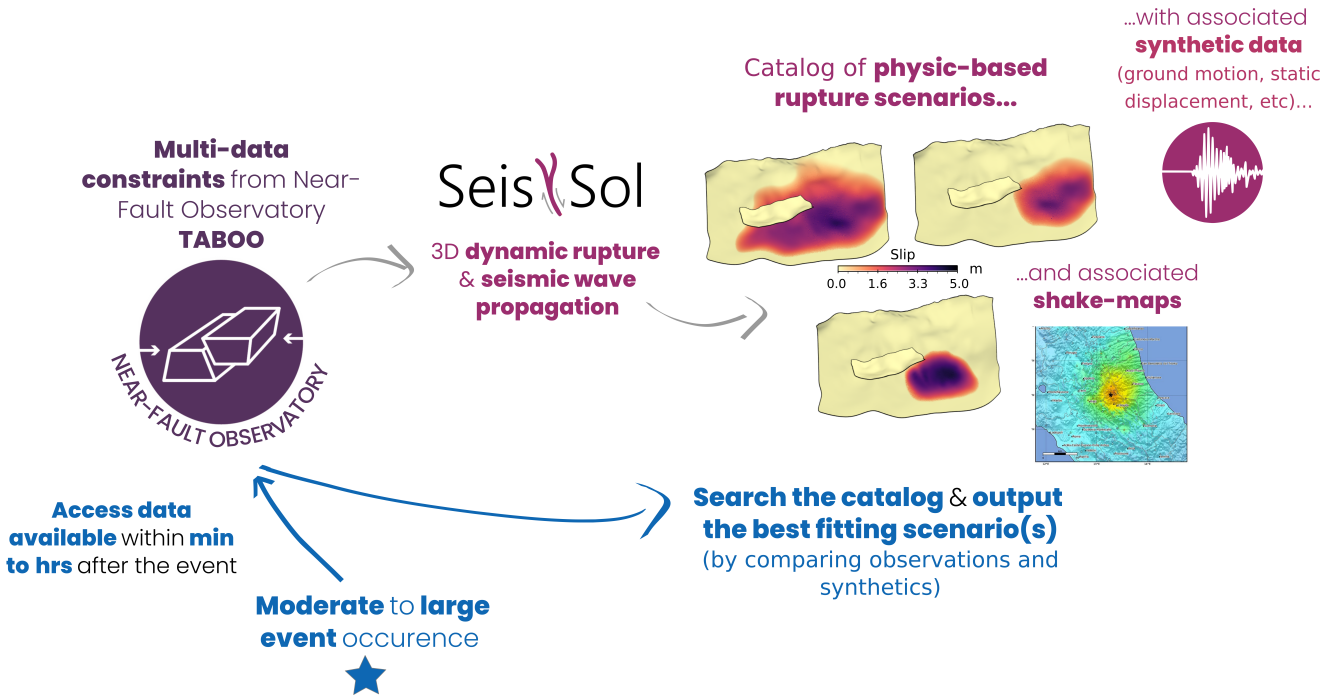


**Figure S12** Schematic representation of the rapid-response dynamic source determination workflow based on a pre-built catalog of scenarios. First, a catalog of physic-based scenarios for the Alto Tiberina fault system (with associated synthetic data and shake-maps) is created (purple part of the graph). Then, in the event of a moderate to large earthquake in the area, the scenario that best represents the event is searched by comparing the observations with the synthetics of every scenario within the catalog (blue part of the graph).

# References

Causse, M., Dalguer, L., and Mai, P. M. Variability of dynamic source parameters inferred from kinematic models of past earthquakes. *Geophysical Journal International*, 196(3):1754–1769, 2014.

Farr, T. G., Rosen, P. A., Caro, E., Crippen, R., Duren, R., Hensley, S., Kobrick, M., Paller, M., Rodriguez, E., Roth, L., et al. The shuttle radar topography mission. *Reviews of geophysics*, 45(2), 2007.

Latorre, D., Mirabella, F., Chiaraluce, L., Trippetta, F., and Lomax, A. Assessment of earthquake locations in 3-D deterministic velocity models: A case study from the Altotiberina Near Fault Observatory (Italy). *Journal of Geophysical Research: Solid Earth*, 121(11):8113–8135, 2016.

Mirabella, F., Ciaccio, M., Barchi, M. R., and Merlini, S. The Gubbio normal fault (Central Italy): geometry, displacement distribution and tectonic evolution. *Journal of Structural Geology*, 26(12):2233–2249, 2004.

Mirabella, F., Brozzetti, F., Lupattelli, A., and Barchi, M. R. Tectonic evolution of a low-angle extensional fault system from restored cross-sections in the Northern Apennines (Italy). *Tectonics*, 30(6), 2011.

NASA Shuttle Radar Topography Mission (SRTM). Shuttle Radar Topography Mission (SRTM) Global. Distributed by OpenTopography, 2013. https://doi.org/10.5069/G9445JDF. Accessed 2025-07-22.

Tinti, E., Spudich, P., and Cocco, M. Earthquake fracture energy inferred from kinematic rupture models on extended faults. *Journal of Geophysical Research: Solid Earth*, 110(B12), 2005.

Valoroso, L., Chiaraluce, L., Di Stefano, R., and Monachesi, G. Mixed-mode slip behavior of the Altotiberina low-angle normal fault system (Northern Apennines, Italy) through high-resolution earthquake locations and repeating events. *Journal of Geophysical Research: Solid Earth*, 122(12):10–220, 2017.